Tenth International Conference on Computational Fluid Dynamics (ICCFD10), Barcelona, Spain, July 9-13, 2018 **ICCFD10-018**

Numerical Analysis on the Mode-Transition of Second-Throat Exhaust Diffuser with Thrust Optimized Parabolic Nozzle

Changsoo Lee*, Kyungjun Choi*, Chongam Kim*,** and Sanghoon Han***
Corresponding author: chongam@snu.ac.kr

* Department of Mechanical and Aerospace Engineering, Seoul National University, Korea.
** Institute of Advanced Aerospace Technology, Seoul National University, Korea.
*** Korea Aerospace Research Institute, Korea.

Abstract: Flow separation in a thrust-optimized parabolic nozzle operating at a high altitude test facility is numerically investigated. The objective of this study is to analyze the effect of a diffuser on flow separation during engine startup and shutdown operations. The 2-D axisymmetric compressible Reynolds Averaged Navier–Stokes equations are solved for the high altitude test of the Korea Space Launch Vehicle-II 3rd-stage engine. Nozzle plume gas modeling, cooled wall boundary condition, and transient chamber inlet condition are implemented for efficient and accurate computations. The computation results show that a secondary flow through a gap between the nozzle exit and the diffuser inlet has strong interaction with the nozzle plume. During the startup operation, the primary and secondary flows form two parallel annular jets. This flow structure enhances the Coanda effect and triggers the transition from free-shock separation to restricted-shock separation. During the shutdown operation, cooling effect of the secondary flow delays the overall flow transition. In addition, the interaction between the primary and secondary flows changes the momentum balance of the flow passing through the separation and reflected shocks, and it leads to the transition from full-flow to restricted-shock separation. In both startup and shutdown operations, complex flow transition in the nozzle induces abnormal behaviors on the diffuser mode-transition.

Keywords: Computation Fluid Dynamics, Liquid Rocket Engine, Rocket Nozzle, High Altitudes Test Facility, Supersonic Diffuser, Flow Separation.

1 Introduction

The rocket nozzles of space launch vehicles exhibit flow separation in over-expanded state. Flow separation has various patterns, and transitions between these patterns can occur during engine startup and shutdown operations. If asymmetric flow separation takes place during the engine operations, asymmetric pressure distribution of the nozzle wall generates lateral forces called side-loads. When side-loads are large and persistent, severe engine breakdown may occur. Indeed, engine breakdowns due to side-loads have been reported in the J-2S engine [1], the Space Shuttle Main Engine (SSME) [2], the Japanese LE-7A engine [3], and the European VULCAIN engine [4], among others. Thus, a clear understanding of flow separation in nozzles is essential for preventing unexpected engine breakdowns and developing high-performance engines.

Many studies have been conducted to investigate flow separation in nozzles. Frey and Hagemann [6] observed that the transition between Free-Shock Separation (FSS; Fig. 1) and Restricted-Shock Separation (RSS; Fig. 2) is one of the main reasons of side-loads. Since then, many researchers have focused on finding the factors that trigger the transition between FSS and RSS. Yonezawa et al. [7] carried out numerical simulations on LE-7, LE-7A, and CTP50-R5-L nozzles to analyze the effect of nozzle geometry. Hagemann

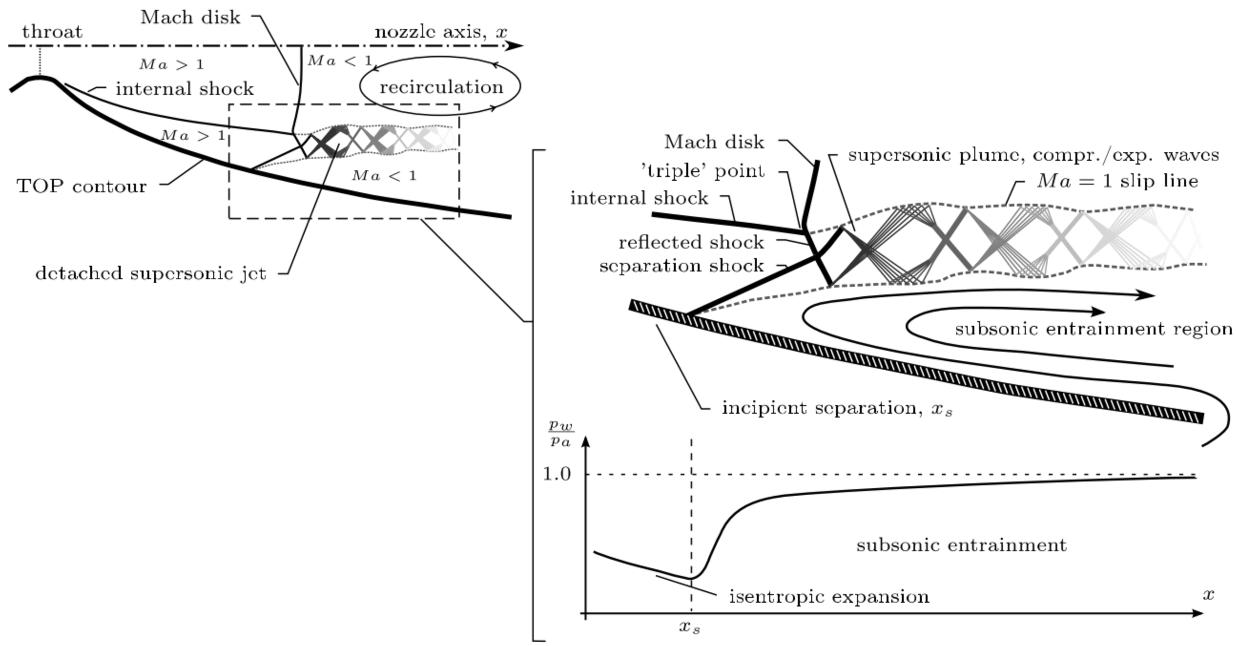

Figure 1: Illustration of the FSS pattern in a TOP nozzle. A typical static wall pressure profile is schematically indicated in the right lower corner. [5]

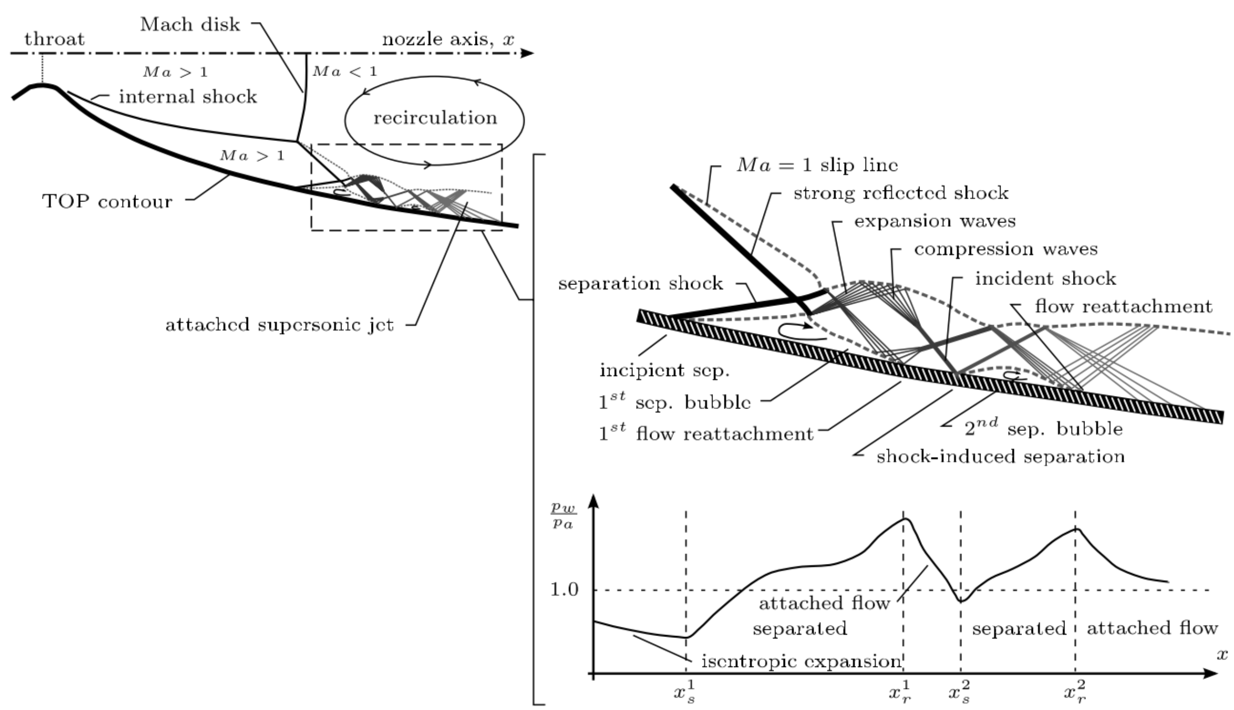

Figure 2: Illustration of the RSS pattern in a TOP nozzle. A typical static wall pressure profile is schematically indicated in the right lower corner .[5]

and Frey [8] confirmed that Thrust-Optimized Parabolic (TOP) nozzles and Compressed Truncated Perfect (CTP) nozzles, which have an internal shock induced by an imperfect wall curvature, are likely to cause the transition between FSS and RSS. Wang et al. [9, 10, 11] carried out intensive numerical studies using the SSME and J-2X engine. The SSME computation results show that regenerative cooling promotes the FSS-to-RSS transition; these results also show that the short startup sequence reduces the amount of time the flow transition stays inside the nozzle, thereby decreasing side-loads. Furthermore, the J-2X engine computation results show that coolant injection in the middle of the nozzle promotes the FSS-to-RSS transition and the asymmetric mass flux of the coolant leads to large side-loads. Jia et al. [12] confirmed that the deflected and reversed supersonic flow by the lower-stage dome causes asymmetric flow separation during the Fire-In-The-Hole staging event. These previous studies show that flow separation in the nozzle is affected by numerous factors such as nozzle shape, cooling system, transient chamber condition, and surrounding structure.

The test environment, such as a High Altitude Test (HAT) facility, is another factor that can affect flow separation in the nozzle. HAT facilities are used for hot-firing tests of upper-stage engines that are equipped with high-area-ratio nozzles that optimize thrust at high altitudes. A diffuser, the most important component of the HAT facility, uses self-evacuation by the entrainment effect of the nozzle plume, as shown in Fig. 3. As the total pressure increases in the engine's combustion chamber, the entrainment effect strengthens, thereby decreasing the vacuum pressure at the diffuser inlet; this state is called diffuser-unstarting mode. When the total pressure rises above the optimum starting pressure, the diffuser is choked by the nozzle plume attached to the diffuser wall and reaches diffuser-starting mode. In this mode, the engine is completely isolated from the effect of the ambient air. The first study of a nozzle installed in a HAT facility was carried out by Verma and Haidn [13]. In their experimental study, they observed that the onset of nitrogen condensation triggers flow transition during the cold gas tests. In addition, they examined how the diffuser delays the onset of condensation, thereby modifying the momentum balance of the flow passing through the separation and reflected shocks, in such a way that only the FSS pattern is favored. To the best of the authors' knowledge, this previous study is the only case that analyzed flow separation in a nozzle considering a HAT facility. However, this study was limited to cold-gas tests using a sub-scale model. Moreover, a detailed flow structure was not fully investigated because the study only analyzed experimental data. Therefore, the objective of this study is to numerically investigate flow separation in an actual full-scale nozzle during hot-firing tests in a HAT facility. For intensive analysis on the detailed flow structure and the effect of the diffuser, rather than asymmetric flow transition, 2-D axisymmetric computations was performed for this study.

The present paper is organized as follows. After the introduction, a detailed model description is given in Section 2. Section 3 presents numerical methodology focused on key components, and Section 4 presents numerical results and discusses flow separation and their transition. Finally, concluding remarks are given in Section 5.

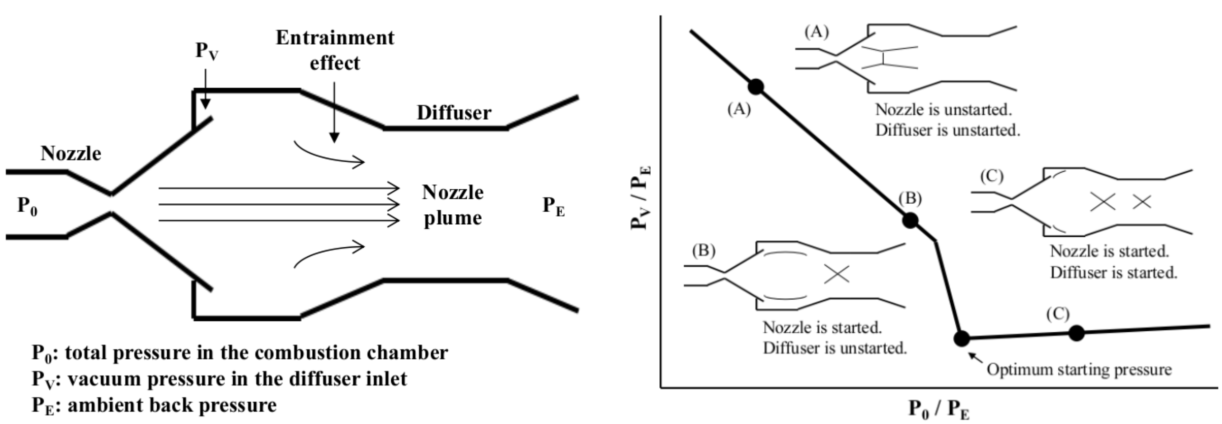

Figure 3: Diffuser mechanism and typical characteristics of diffuser

2 Model Description

The target model is the Korea Space Launch Vehicle-II (KSLV-II) 3rd-stage rocket engine developed by Korea Aerospace Research Institute (KARI). The engine is equipped with a TOP nozzle with an area ratio of 94.5 to maximize thrust at high altitudes. The detailed specification of the KSLV-II 3rd-stage rocket engine is given in Table 1.

A Second Throat Exhaust Diffuser (STED) is used as the HAT facility for the KSLV-II 3rd-stage rocket engine. When designing the test facility, a gap was set between the nozzle exit and the diffuser inlet to improve the structural stability. Figure 4 shows the characteristics of the test facility depending on the existence of the gap. If the nozzle and diffuser are tightly connected, a structural vibration from the nozzle or the diffuser can propagate throughout the whole test facility. In contrast, the propagation of the structural vibration is avoided when there is a gap, and the structural stability is consequently improved. However, the driving force of the entrainment effect is partially consumed to induce a secondary flow through the gap. Therefore, the self-evacuation performance of the diffuser is degraded. In addition, the secondary flow interacts with the nozzle plume, which could affect the separation pattern of the nozzle plume. Therefore, the effect of the secondary flow has to be investigated.

The two models shown in Fig. 5 are selected for the computations to investigate the effect of the secondary

Table 1: Spec. of KSLV-II 3rd-stage rocket engine

List	Unit	Spec.
Power cycle	-	Gas-generator cycle
Cooling system	-	Regenerative cooling
Oxidizer/fuel	-	Liquid oxygen/Kerosene
Nozzle shape	-	Thrust-Optimized Parabolic
Nozzle area ratio	-	94.5
Max. chamber pressure	Bar	70.0
Nozzle exit pressure	Bar	0.05
Mass flow rate	kg/s	21.5
Thrust in a vacuum	tonf	7.0

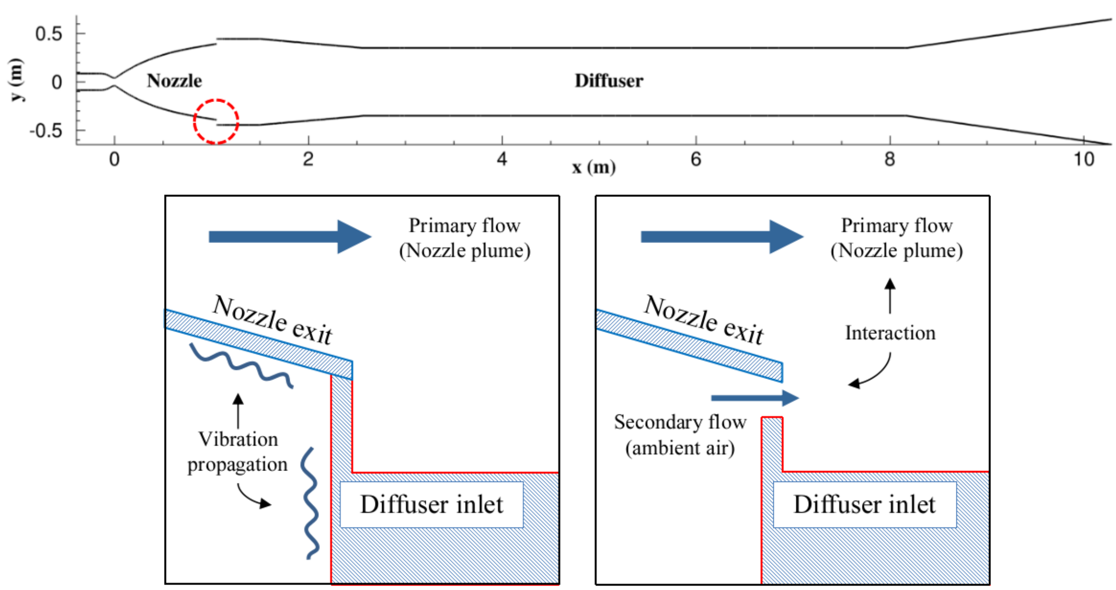

Figure 4: Geometry of the nozzle and the diffuser (top). Schematics of the nozzle exit and the diffuser inlet: without gap (bottom left), with gap (bottom right)

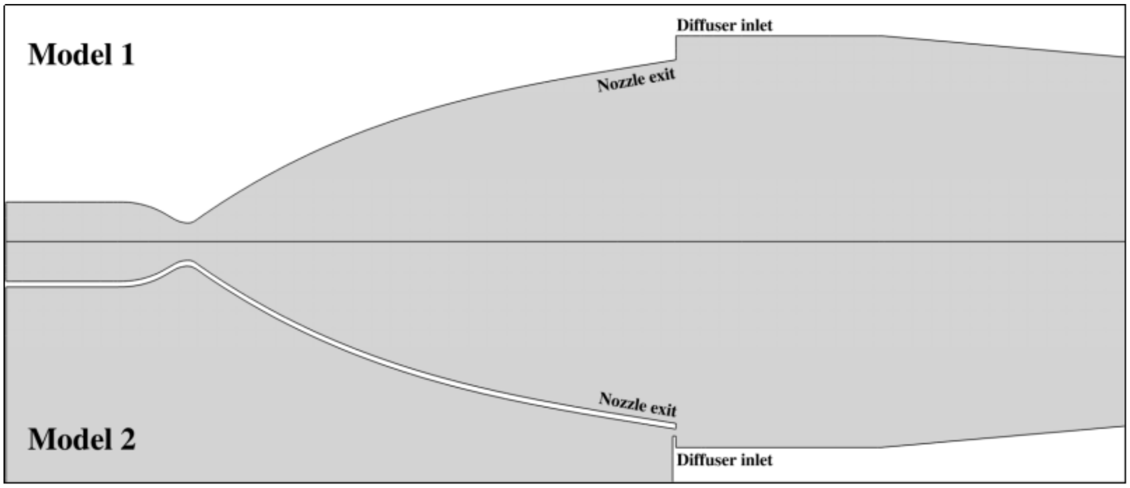

Figure 5: Geometry of Model 1 without gap (top) and Model 2 with 15 mm gap (bottom)

flow through the gap. Model 1 has no gap between the nozzle exit and the diffuser inlet; this model is different from the experiment but selected as a baseline. Model 2 has a gap between the nozzle exit and the diffuser inlet, which is similar to the experiment. Although the gap in the experiment is designed to be adjustable in the range of 10–20 mm, the gap size is fixed at 15 mm in this study to reduce numerical complexity.

3 Numerical Methodology

Numerical simulations are carried out using an in-house solver based on 2-D axisymmetric compressible Reynolds Averaged Navier–Stokes equations. The detailed numerical methods are listed in Table 2.

3.1 Nozzle plume gas modeling

Nozzle plume gases are modeled as one-averaged equivalent gas to reduce the computational cost. The fidelity of the thermodynamic model is improved by modeling the specific heat capacity of the gas as a function of the static temperature. All gas properties are obtained from the NASA Chemical Equilibrium with Applications (CEA) program.

Table 2: Lists of numerical methods

List	Contents
Dimension	2-D axisymmetric
Grid system	Unstructured mixed grid
Equation of state	Calorically imperfect ideal gas
Spatial discretization	AUSMPW+ [14]
Cell gradient method	Weighted least-square with extended stencil
Face gradient method	Face-tangent augmented cell-face method
Limiter function	Modified Venkatakrishnan with MLP [15, 16] frame
Temporal discretization	BDF2 with Block-LUSGS [17] (using 1st order jacobian)
Time step	1.0e-5
Turbulence model	$k - w$ SST (2003) [18]
Compressibility correction	Sarkar's pressure-dilatation [19]

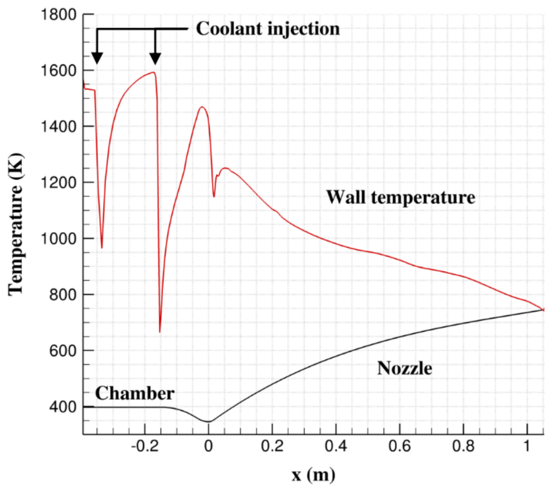

Figure 6: Wall temperature distribution of the chamber and the nozzle

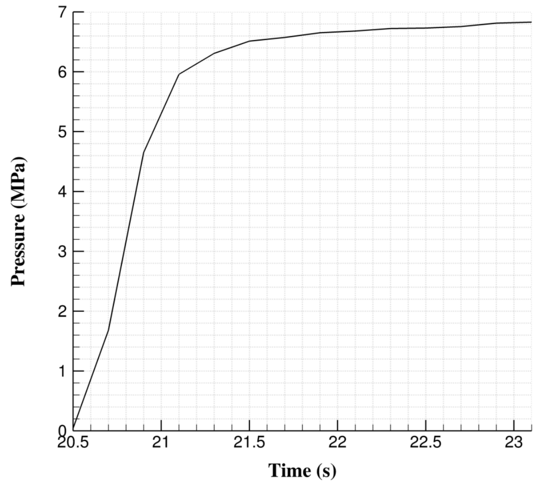

Figure 7: Pressure history of KSLV-II 3rd-stage rocket engine during the startup operation

3.2 Cooled wall boundary condition

The engine's cooling system is an essential element for protecting the engine structure. In addition, the wall temperature distribution that is changed by the cooling system greatly influences the flow structure in the nozzle [9]. Therefore, the cooling system has to be considered for the numerical analysis.

The main cooling system of the KSLV-II 3rd-stage rocket engine is regenerative cooling and is used for both the chamber and the nozzle. As a sub-cooling system, the chamber also uses film-cooling, which injects coolant to enhance the cooling effect. Figure 6 shows the wall temperature distribution of the chamber and nozzle from the experiment. The regenerative cooling effect keeps the overall wall temperature of the chamber and nozzle below 1600 K. In the case of the chamber, there are two sudden drops in the wall temperature due to coolant injection. These cooling effects are taken into account by implementing a cooled wall boundary condition for the computations. The wall temperature distribution of the chamber and nozzle are applied based on the experimental data. The mass flux of the coolant injected into the chamber is ignored because the coolant has a very low mass flux compared to the nozzle plume.

3.3 Transient chamber inlet condition

The chamber inlet pressure and temperature changes should be applied to simulate the startup and shutdown operations. However, only the startup pressure history shown in Fig. 7 was measured in the experiment. Therefore, the chamber inlet pressure and temperature histories were simply modeled by referring to the J2-X engine data [10].

Figures 8 and 9 show the chamber inlet pressure and temperature histories which are modeled for simulating the engine operations. The maximum pressure and temperature are 7 MPa and 3642.69 K, respectively. During the startup operation, the chamber inlet pressure and temperature are ramped up for 0.500 and 0.250s, respectively. During the shutdown operation, both the chamber inlet pressure and temperature are ramped down for 0.250s.

3.4 Computational grid generation

Wang [20] showed that a quadrilateral-cell dominated mixed grid has a better performance than a triangle-cell dominated mixed grid in accuracy and efficiency, on the nozzle's flow physics. Several grids were generated based on the results of that study and a grid convergence study was then conducted. Figure 10 shows the final grid of Model 2 used for the computations; the total number of cells is 64,731, and the grid has enough

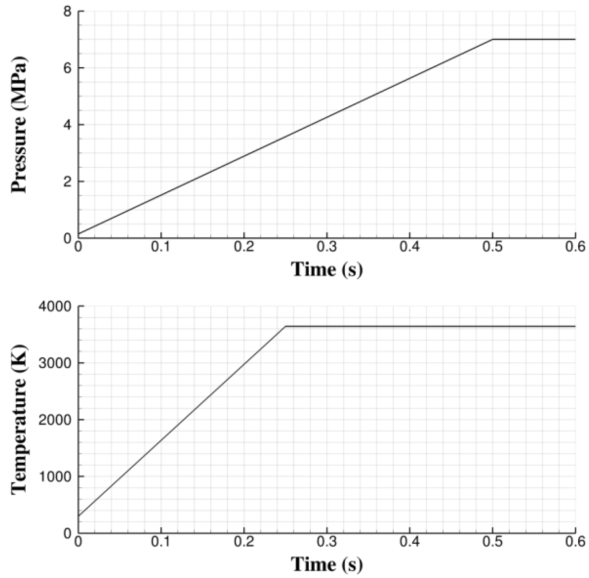

Figure 8: Modeling of the transient chamber inlet condition for the startup operation

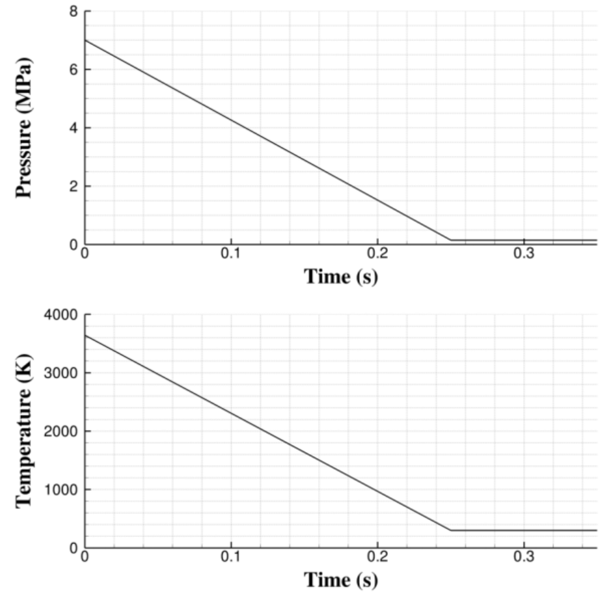

Figure 9: Modeling of the transient chamber inlet condition for the shutdown operation

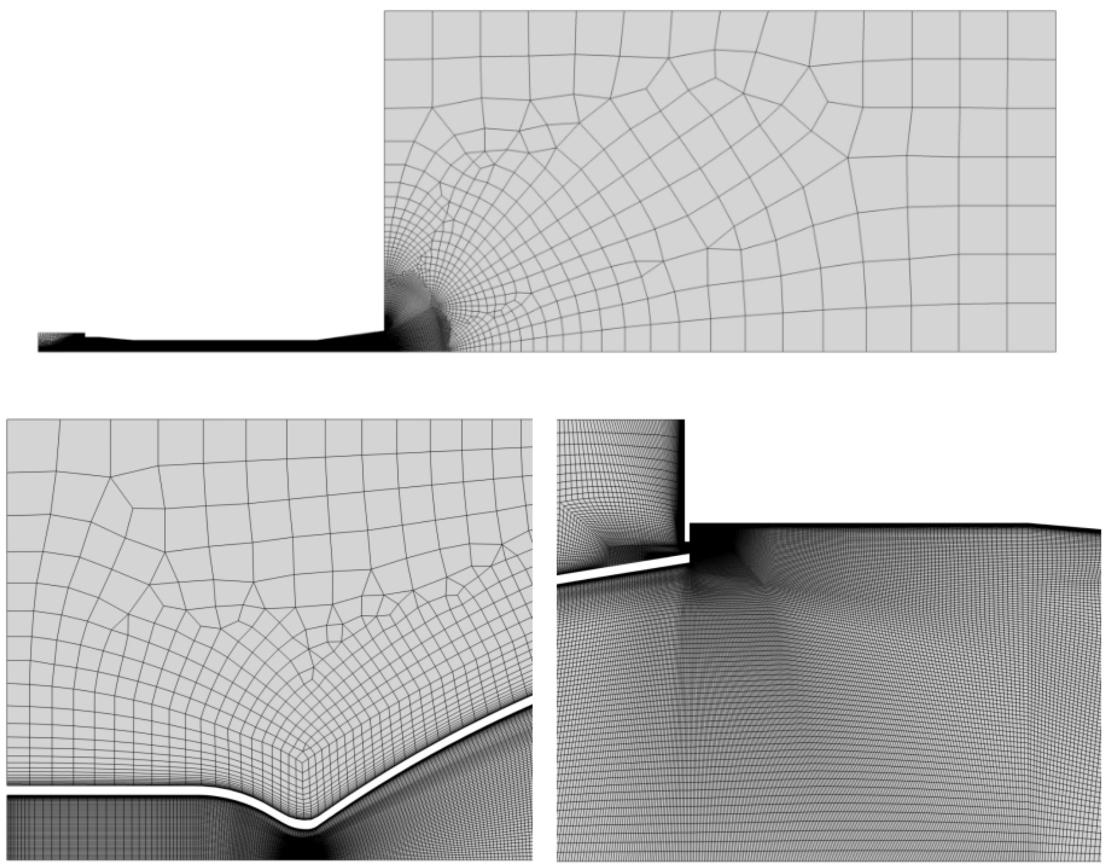

Figure 10: Unstructured mixed grid of Model 2

far-field space to ensure the elliptic characteristics at the diffuser exit. A grid of Model 1 is not shown in this paper but has similar quality to the grid of Model 2; the total number of cells is 57,887, and the grid has enough far-field space.

4 Results and Discussion

4.1 Full-flowing condition

Computation with full-flowing condition using Model 2 was performed to validate the solver. Figure 11 shows the Mach number distribution and the wall pressure distribution in the nozzle. Internal shock, which is a typical flow characteristic of TOP nozzles, is induced downstream of the nozzle throat. In addition, the wall pressure distribution is almost the same as the experimental data. This result shows that the gas modeling in Section 3.1 and the cooled wall boundary condition in Section 3.2 are suitable for simulating

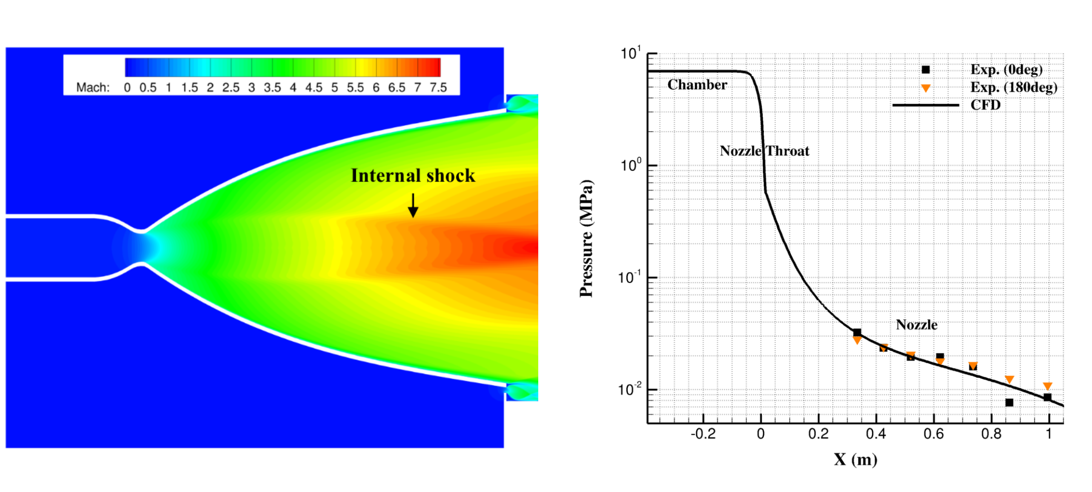

Figure 11: Mach number distribution inside the nozzle (left), and the wall pressure distribution along the nozzle wall (right)

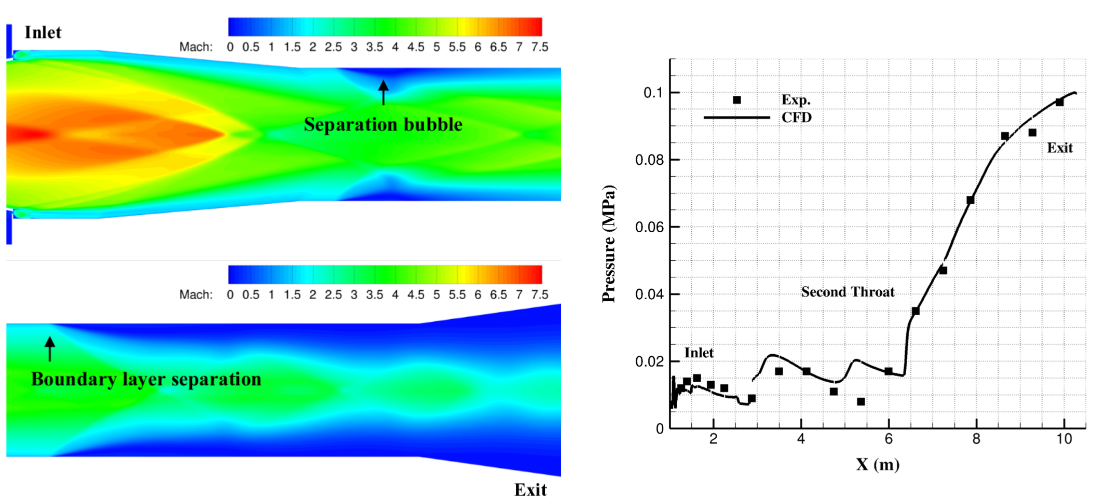

Figure 12: Mach number distribution inside the diffuser (left), and the wall pressure distribution along the diffuser wall (right)

the nozzle plume.

Figure 12 shows the Mach number distribution and the wall pressure distribution in the diffuser. A separation bubble is formed at the entrance of the diffuser throat, which results in a sudden rise in the wall pressure. Likewise, the experimental data shows that the wall pressure rises by the separation bubble at the same position. However, the location of the boundary layer separation near the diffuser exit differs from the experimental data; the main reason for this difference is related to the single gas assumption. In reality, the ambient air has different gas properties from the nozzle plume. However, the actual gas properties of the ambient air are not considered, in order to reduce the numerical complexity. Therefore, the location of the boundary layer separation differs in the experimental data due to the large influence of the ambient air. However, there is no significant difference in the upstream, where the ambient air's influence is small.

4.2 Engine startup operation

Figure 13 shows the computed time-varying Mach number distributions during the startup operation. The vacuum pressure histories measured at the diffuser inlet are as shown in Fig. 14. Until around 0.310s, Model 1 and 2 both show the FSS pattern (Fig. 13a), and the vacuum pressure gradually decreases in both. In the FSS pattern, the nozzle plume, named the primary flow, takes the form of annular jet. The annular jet has a larger entrainment rate at the center and so this jet is merged into a single round jet. This jet structure creates a recirculation zone downstream of the Mach disk. This flow physics basically governs the flow structure in both models. However, Model 2 has additional flow physics caused by the secondary flow, which becomes a supersonic jet due to gap choking and forms an outer annular jet that surrounds the primary flow. The flow structure with two parallel annular jets has a large entrainment effect at the region between the two jets [21, 22]. Therefore, Model 2 has lower pressure at the region between the primary flow and the nozzle wall than Model 1, as shown in Fig. 15. In addition, this low pressure makes the two annular jets merge into a single annular jet, as shown in Fig. 16.

Between 0.310 and 0.360s, Model 1 maintains the FSS pattern, but Model 2 undergoes the FSS-to-RSS transition as shown in Fig. 13 a–b. The mechanism of the FSS-to-RSS transition is explainable by the Coanda effect [9, 10]. When a jet or sheet of fluid is injected into another fluid, the jet entrains the surrounding fluid, which causes low pressure around the jet. If a wall is placed close, the entrainment effect at the region between the jet and the wall increases and the jet tends to be attached to the wall. However, the low pressure in the recirculation zone in Model 1 resists the Coanda effect and thus keeps the primary flow away from the nozzle wall. Meanwhile, the interaction with the secondary flow in Model 2 promotes the Coanda effect by lowering the pressure at the region between the primary flow and the nozzle wall. Consequently, the primary flow bends to the nozzle wall, and gets closer to the secondary flow, which in turn strengthen the interaction between the primary and secondary flows. This feedback process induces the FSS-to-RSS transition, during which Model 2 shows non-smooth vacuum pressure behavior at 0.330–0.360s, as shown in Fig. 14. During this transition, the primary flow is attached to the nozzle wall and creates a series of separation bubbles, resulting in the vacuum pressure fluctuations. Soon after, the primary flow temporarily adheres to the diffuser wall. At that point, the secondary flow is blocked and the vacuum pressure rises rapidly. In addition, the transition to the RSS pattern opens the recirculation zone, which increases the pressure downstream of the Mach disk through the effect of high ambient air pressure. The high back-pressure pushes the Mach disk back to the upstream, which delays the evolution of the entire flow structure.

After 0.360s, Model 1 shows a relatively simple flow transition. As the total pressure of the chamber rises gradually, the flow separation point moves downstream. At around 0.380s, the flow separation point reaches the nozzle exit and the Mach disk exits the nozzle. This transition is the FSS-to-full-flow transition (Fig. 13b–c). Immediately after this transition, the diffuser is choked by the primary flow impinging on the diffuser wall, and Model 1 reaches the diffuser-starting mode (Fig. 13d). This flow structure in the diffuser-starting mode continues until the end of the computation (Fig. 13d–f). The vacuum pressure history during the mode-transition process follows the diffuser's typical characteristics.

In contrast, Model 2 goes through a complex flow transition after 0.360s. At 0.380s, the Mach disk is still located inside the nozzle due to the high pressure of the open recirculation zone and the first separation bubble does not reach the nozzle exit (Fig. 13c). The reattachment point of the first separation bubble eventually reaches the nozzle exit at 0.415s, as shown in Fig. 17. At that point, the high pressure of this

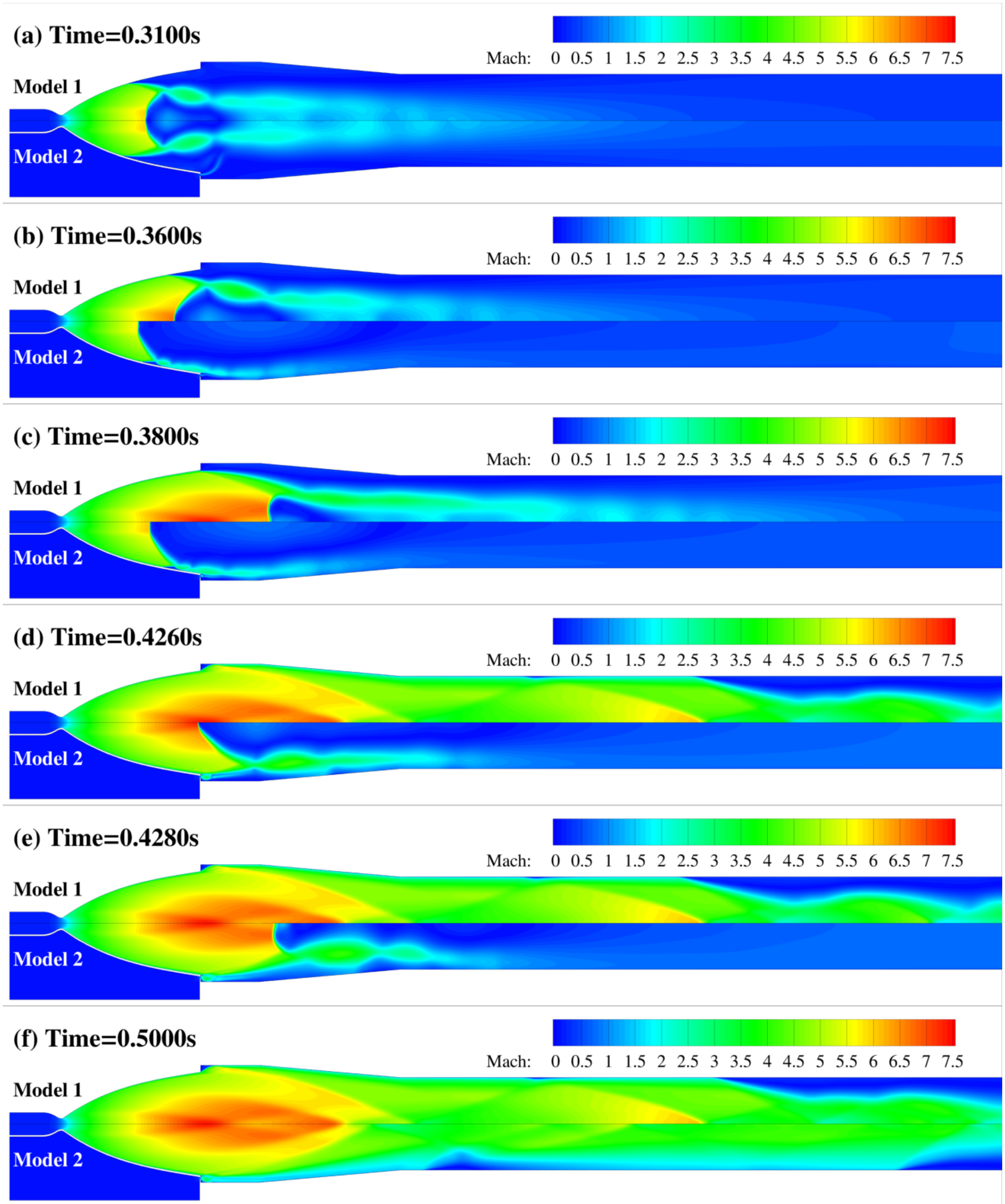

Figure 13: Mach number distribution during the startup operation without gap (top side), with 15mm gap (bottom side)

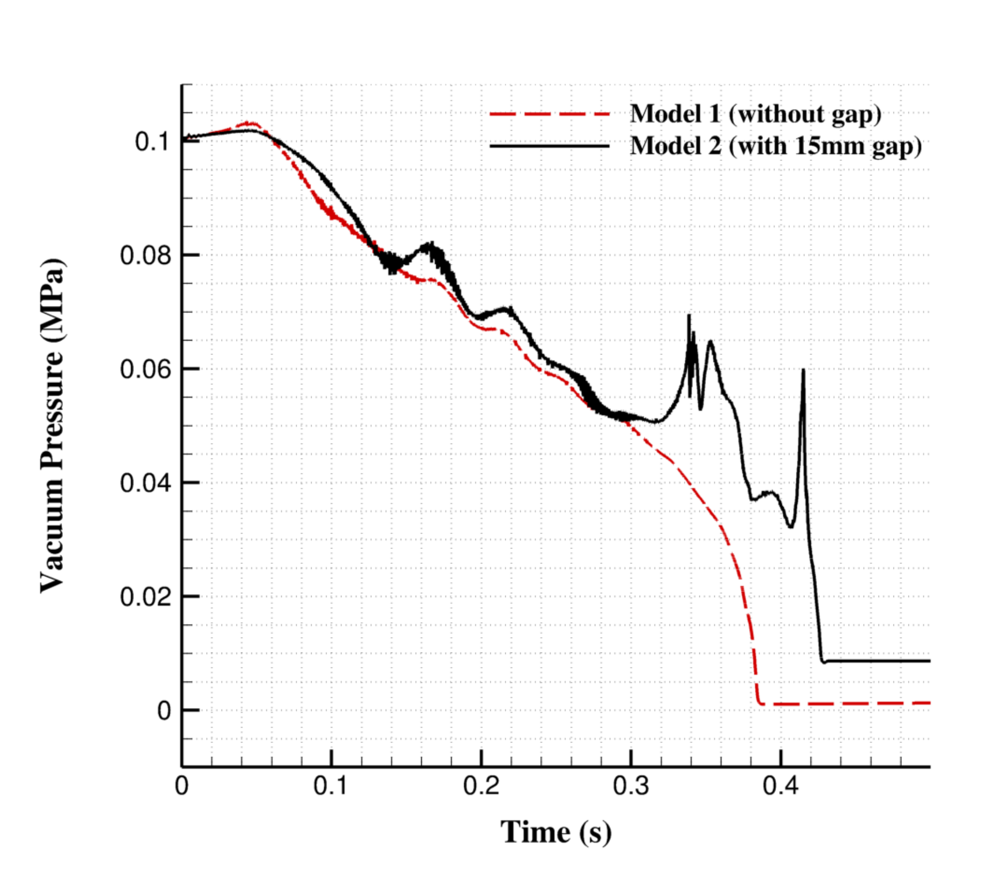

Figure 14: Vacuum pressure history during the startup operation

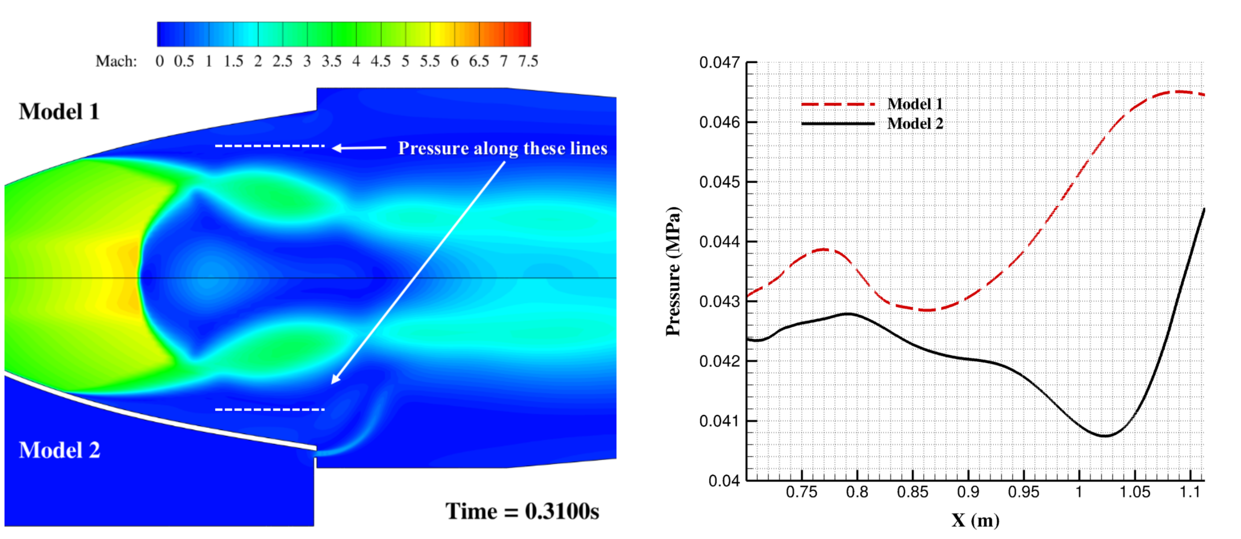

Figure 15: Pressure distribution between the primary flow and the the nozzle wall

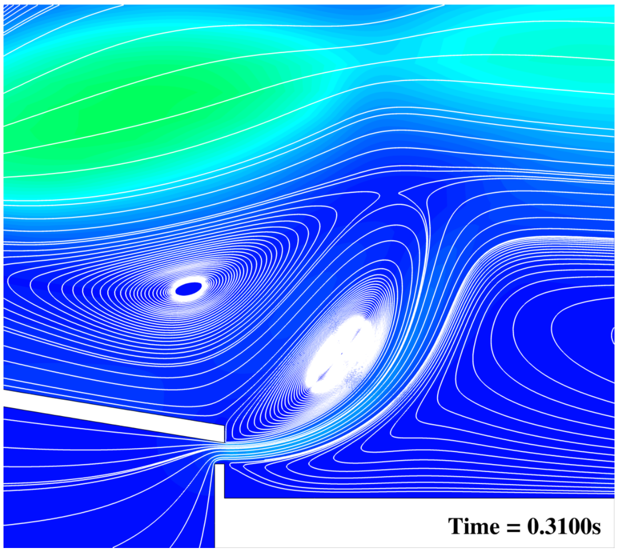

Figure 16: Mach number distribution and streamline (white line) near the nozzle exit at 0.310s

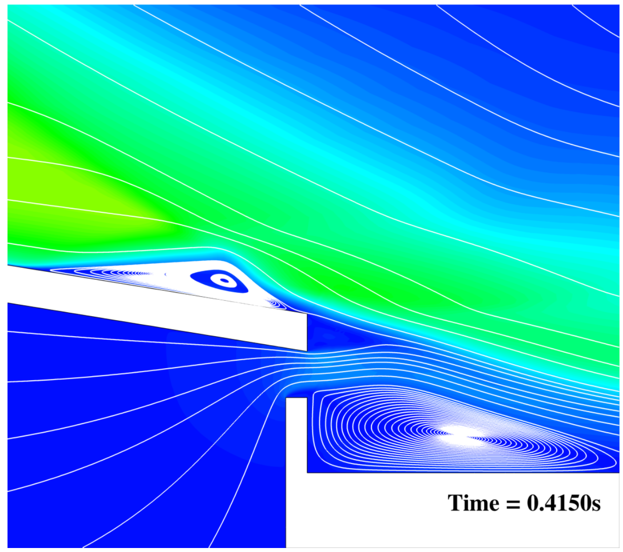

Figure 17: Mach number distribution and streamline (white line) near the nozzle exit at 0.415s

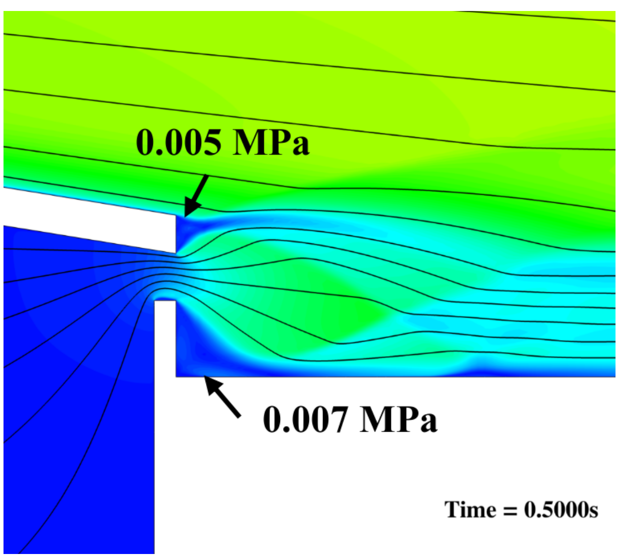

Figure 18: Mach number distribution and streamline (black line) near the nozzle exit at 0.500s

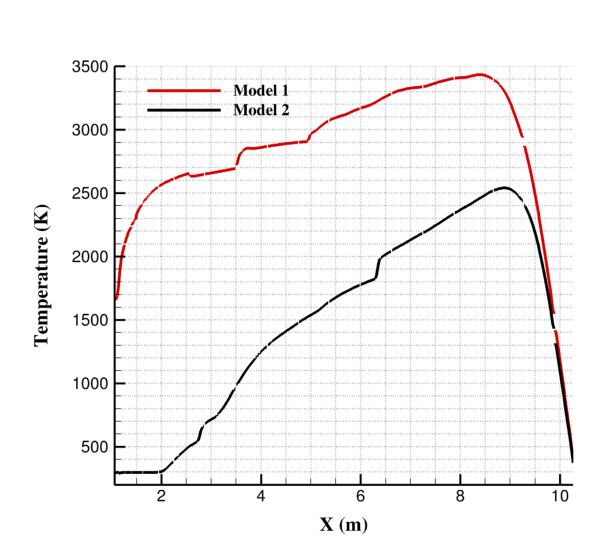

Figure 19: Temperature distribution at the diffuser wall

reattachment point results in a vacuum pressure peak, as shown in Fig. 14. After all the separation bubbles have exited, the primary and secondary flows are merged into a single flow at the nozzle exit. Soon after, the Mach disk exits the nozzle. Figure 13c–e shows the RSS-to-full-flow transition described above. The secondary flow impinges on the diffuser wall after this transition. Then, the diffuser choked by the primary and secondary flows reaches the diffuser-starting mode (Fig. 13f).

Each model has a different flow structure in the diffuser-starting mode. Model 1's primary flow continues to expand until it impinges on the diffuser wall. This under-expanded flow condition reduces the vacuum pressure to 0.001 MPa. In Model 2, a portion of the secondary flow expanding inward merges with the primary flow at the nozzle exit, and the remaining portion expanding outward impinges on the diffuser wall (Fig. 18). Model 2's vacuum pressure is higher than Model 1 due to the lower expansion rate at the diffuser inlet, as shown in Fig. 14. In addition, there is a difference in the location of the boundary layer separation. Figure 13f shows that Model 2's boundary layer separation is shifted toward the diffuser exit compared to Model 1; this difference is caused by the film-cooling effect of the secondary flow. The secondary flow is induced from the ambient air, which means that this flow has a very low temperature compared to the primary flow. Consequently, the secondary flow acts as a coolant and lowers the diffuser wall temperature. Figure 19 shows that Model 2's diffuser wall temperature is much lower than Model 1 through the film-cooling effect. This lower temperature leads to higher density and higher momentum near the wall. Therefore, the boundary layer becomes thinner, which delays the boundary layer separation [23, 24].

4.3 Engine shutdown operation

Figure 20 shows the computed time-varying Mach number distribution during the shutdown operation. The vacuum pressure histories measured at the diffuser inlet are as shown in Fig. 21. In Model 1, the transition to the diffuser-unstarting mode occurs when the primary flow is detached from the diffuser wall. Figure 21 shows that Model 1's vacuum pressure is increased rapidly by the effect of the ambient air at this point. Soon after, the Mach disk comes inside the nozzle and the full-flow-to-FSS transition occurs. Figure 20a–b shows the change in the flow structure during this transition.

In Model 2, the film-cooling effect of the secondary flow delays the transition to the diffuser-unstarting mode. Figure 20a shows that Model 2's separation point is located further downstream than Model 1 at the same moment. Even when the transition to the diffuser-unstarting mode occurs in Model 1, Model 2 maintains the diffuser-starting mode (Fig. 20b). Model 2 eventually reaches the diffuser-unstarting mode at around 0.129s due to the secondary flow detaching from the diffuser wall. Although the vacuum pressure increases after this transition, the nozzle exit, which is isolated from the ambient air by the primary and secondary flows, keeps the pressure low as shown in Fig. 22. This low pressure fixes the separation point of the primary flow at the nozzle exit, which leads to a different momentum balance from Model 1. Figure 23 shows the difference in the momentum balance between the models when the Mach disk is in a similar position. In Model 1, the magnitude of the flow momentum across the separation shock is similar to that of the flow momentum across the reflected shock. This momentum balance combined with the low pressure of the recirculation zone results in a transition to the FSS pattern. In Model 2, however, the flow momentum across the separation shock has a much smaller magnitude than the flow momentum across the reflected shock due to the primary flow's fixed separation point. As the Mach disk moves upstream, the momentum difference between two flows increases, inducing the full-flow-to-RSS transition. In addition, the transition to the RSS pattern causes the vacuum pressure fluctuation shown in Fig. 21, just as it did during the startup operation. Figure 20b–d shows the transition process described above.

Following the transition to the diffuser-unstarting mode, Model 1 and 2 have the FSS and RSS patterns, respectively (Fig. 20d). As the chamber pressure decreases, the flow momentum across the reflected shock becomes smaller than before due to the geometric features, the high curvature near the nozzle throat and the close proximity between the internal shock and the nozzle wall. This change in momentum balance increases the stability of Model 1's FSS pattern. However, this momentum balance change in Model 2 destabilizes the RSS pattern, which increases the size of the first separation bubble (Fig. 20e). As the size of the first separation bubble increases, the first reattachment point moves downstream along the nozzle wall and finally reaches the nozzle exit at 0.159s, as shown in Fig. 24. The high pressure at this reattachment point results in the vacuum pressure peak shown in Fig. 21. Subsequently, the flow structure is transformed to the FSS pattern. Figure 20d–f shows that Model 2 undergoes the RSS-to-FSS transition.

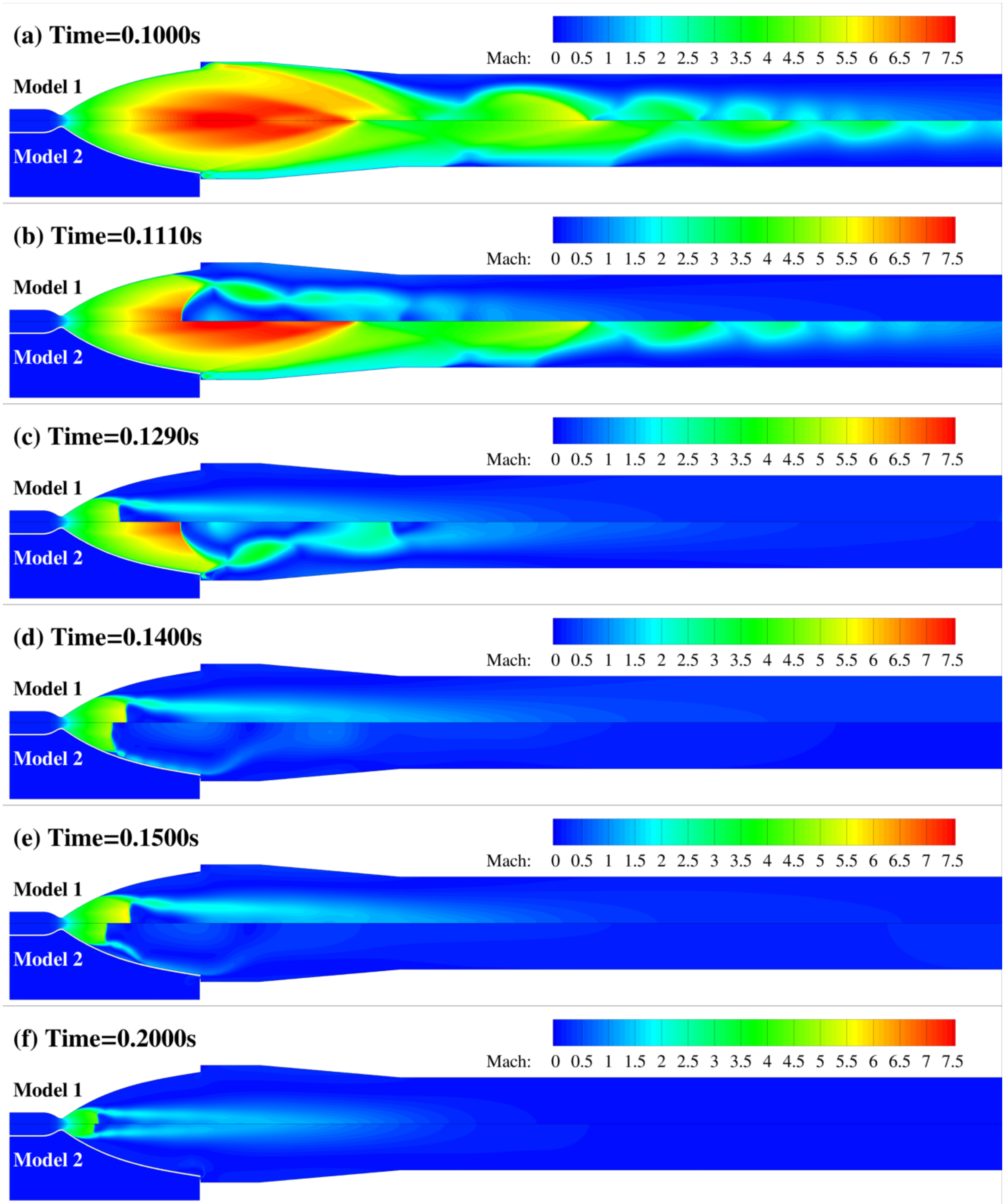

Figure 20: Mach number distribution during the shutdown operation without gap (top side), with 15mm gap (bottom side)

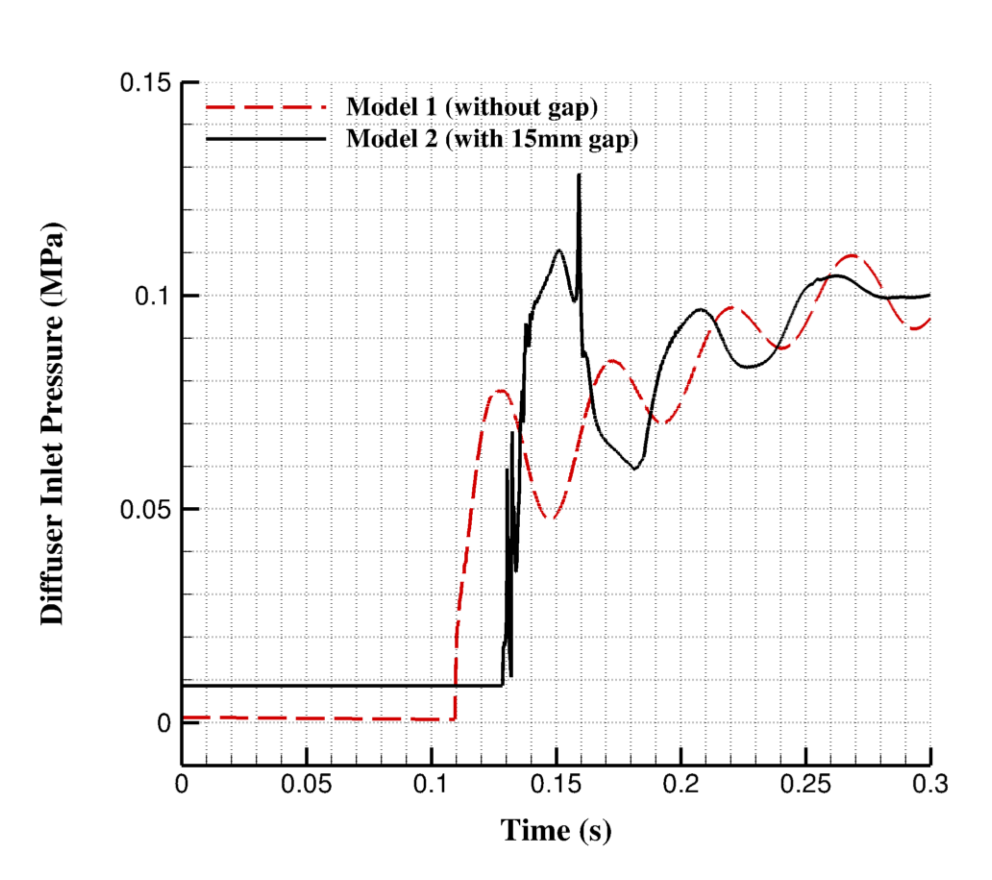

Figure 21: Vacuum pressure history during the shutdown operation

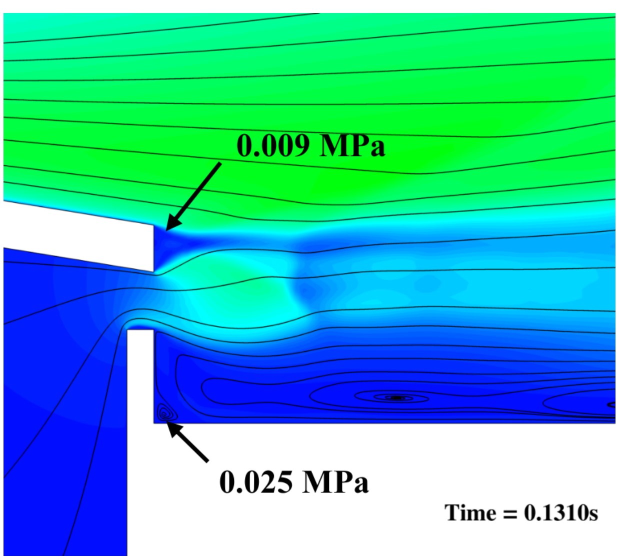

Figure 22: Mach number distribution and streamline (black line) near the nozzle exit at 0.131s

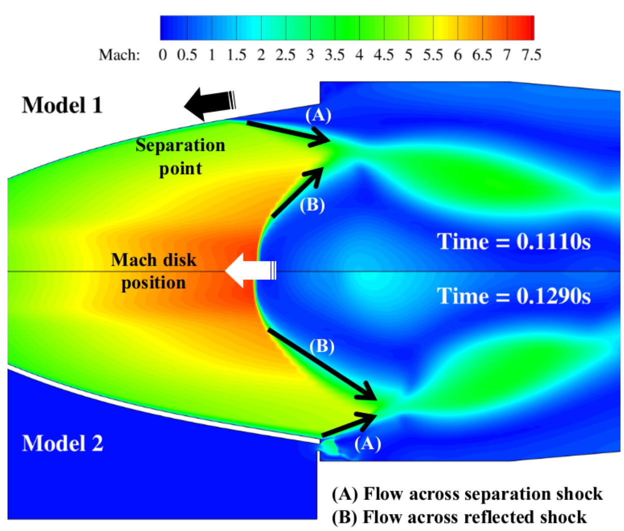

Figure 23: Comparison of Mach number distribution and flow structure - model 1 at 0.111s (top), model 2 at 0.129s (bottom)

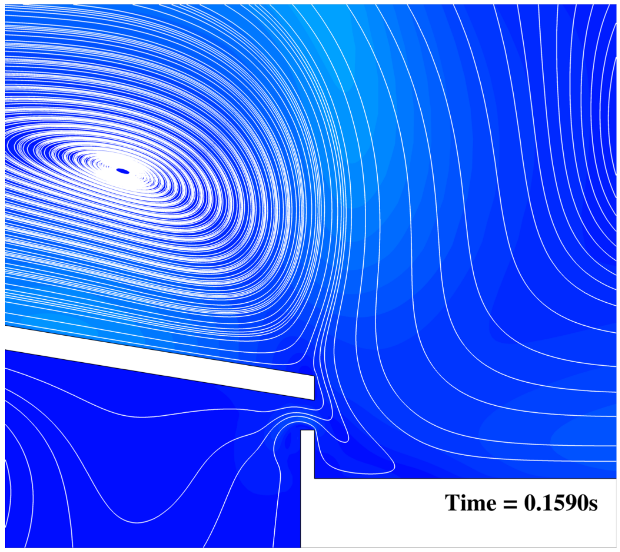

Figure 24: Mach number distribution and streamline (white line) near the nozzle exit at 0.159s

5 Conclusions

Flow separation in the KSLV-II 3rd-stage rocket engine operating at the HAT facility are numerically investigated to analyze the effect of the diffuser. The two models are selected depending on the existence of the gap between the nozzle exit and the diffuser inlet; Model 1 has no gap and Model 2 has a 15 mm gap. The nozzle plume gas modeling, the cooled wall boundary condition, and the transient chamber inlet condition are implemented for efficient and accurate computations. The result with full-flowing condition shows that the numerical methods used in computations are suitable for simulating flow phenomena in the nozzle and the diffuser. During the engine startup and shutdown operations, the secondary flow through the gap in Model 2 shows strong interaction with the nozzle plume, named the primary flow. During the startup operation, only the FSS-to-full-flow transition occurs in Model 1 for reaching the diffuser-starting mode. In Model 2, the primary flow and secondary flows form two parallel annular jets. This flow structure enhances the Coanda effect and triggers the FSS-to-RSS transition, which delays the evolution of the overall flow structure. Subsequently, Model 2 undergoes the RSS-to-full-flow transition for reaching the diffuser-starting mode. During the shutdown operation, Model 1 shows only the full-flow-to-FSS transition, following the transition to the diffuser-unstarting mode. In Model 2, the cooling effect of the secondary flow delays the transition to the diffuser unstarting-mode. In addition, the secondary flow modifies the momentum balance of the flow passing through the separation and reflected shocks and leads to the full-flow-to-RSS transition. Subsequently, the RSS-to-FSS transition occurs due to the geometric features of the nozzle. In both startup and shutdown operations, complex flow transition in Model 2 results in the non-smooth vacuum pressure behaviors at the diffuser inlet.

The results from this study therefore shows that secondary flow induced by the diffusers cause complex flow separation, degrading the diffuser performance. These undesirable flow phenomena could lead to engine breakdowns during hot-firing tests at the HAT facility. This study will be continued to 3-D computations in order to analyze asymmetric flow separation, generating side-loads.

Acknowledgments

This study was performed as a part of the Korea Space Launch Vehicle (KSLV-II) development project (NRF-2017M1A3A1A02014265). The authors also appreciate the support by the Advanced Research Center Program (NRF-2013R1A5A1073861) and by the Korea Institute of Science and Technology Information (KISTI) supercomputing center (KSC-2017-G2-0004).

References

[1] L. H. Nave and G. A. Coffey. Sea level side loads in high-area-ratio rocket engines. In *9th Propulsion Conference*. American Institute of Aeronautics and Astronautics, 1973.

[2] H. A. Cikanek. Characteristics of Space Shuttle Main Engine failures. In *23rd Joint Propulsion Conference*, Joint Propulsion Conferences. American Institute of Aeronautics and Astronautics, jun 1987.

[3] Y. Watanabe, N. Sakazume, and M. Tsuboi. LE-7A Engine Nozzle Problems during Transient Operations. In *38th AIAA/ASME/SAE/ASEE Joint Propulsion Conference & Exhibit*, Joint Propulsion Conferences. American Institute of Aeronautics and Astronautics, jul 2002.

[4] L. Winterfeldt, B. Laumert, R. Tano, Ph. James, F. Geneau, R. Blasi, and G. Hagemann. Redesign of the Vulcain 2 Nozzle Extension. In *41st AIAA/ASME/SAE/ASEE Joint Propulsion Conference & Exhibit*, Joint Propulsion Conferences. American Institute of Aeronautics and Astronautics, jul 2005.

[5] W. J. Baars, C. E. Tinney, J. H. Ruf, A. M. Brown, and D. M. McDaniels. Wall Pressure Unsteadiness and Side Loads in Overexpanded Rocket Nozzles. *AIAA Journal*, 50(1):61–73, jan 2012.

[6] M. Frey and G. Hagemann. Restricted Shock Separation in Rocket Nozzles. *Journal of Propulsion and Power*, 16(3):478–484, may 2000.

[7] K. Yonezawa, K. Yokota, Y. Tsujimoto, N. Sakazume, and Y. Watanabe. Three Dimensional Unsteady Flow Simulation of Compressed Truncated Perfect Nozzles. In *38th AIAA/ASME/SAE/ASEE Joint Propulsion Conference & Exhibit*. American Institute of Aeronautics and Astronautics, 2002.

[8] G. Hagemann and M. Frey. Shock pattern in the plume of rocket nozzles: needs for design consideration. *Shock Waves*, 17(6):387–395, 2008.

[9] T.-S. Wang. Transient three-dimensional startup side load analysis of a regeneratively cooled nozzle. *Shock Waves*, 19(3):251–264, 2009.

[10] T.-S. Wang and M. Guidos. Transient Three-Dimensional Side-Load Analysis of a Film-Cooled Nozzle. *Journal of Propulsion and Power*, 25(6):1272–1280, 2009.

[11] T.-S. Wang, J. Lin, J. Ruf, M. Guidos, and G. C. Cheng. Effect of Coolant Flow Distribution on Transient Side-Load of Film Cooled Nozzles. *Journal of Propulsion and Power*, 28(5):1081–1090, 2012.

[12] R. Jia, Z. Jiang, and W. Zhang. Numerical analysis of flow separation and side loads of a conical nozzle during staging. *Proceedings of the Institution of Mechanical Engineers, Part G: Journal of Aerospace Engineering*, 230(5):845–855, aug 2015.

[13] S. B. Verma and O. Haidn. Cold Gas Testing of Thrust-Optimized Parabolic Nozzle in a High-Altitude Test Facility. *Journal of Propulsion and Power*, 27(6):1238–1246, nov 2011.

[14] K. H. Kim, C. Kim, and O.-H. Rho. Methods for the Accurate Computations of Hypersonic Flows. *Journal of Computational Physics*, 174(1):38–80, 2001.

[15] J. S. Park, S.-H. Yoon, and C. Kim. Multi-dimensional limiting process for hyperbolic conservation laws on unstructured grids. *Journal of Computational Physics*, 229(3):788–812, 2010.

[16] J. S. Park and C. Kim. Multi-dimensional limiting process for finite volume methods on unstructured grids. *Computers & Fluids*, 65:8–24, 2012.

[17] R. F. Chen and Z. J. Wang. Fast, Block Lower-Upper Symmetric Gauss-Seidel Scheme for Arbitrary Grids. *AIAA Journal*, 38(12):2238–2245, 2000.

[18] F. R. Menter, M. Kuntz, and R. Langtry. Ten years of industrial experience with the SST turbulence model. *Turbulence, heat and mass transfer*, 4(1), 2003.

[19] S. Sarkar. The pressureâĂŞdilatation correlation in compressible flows. *Physics of Fluids A: Fluid Dynamics*, 4(12):2674–2682, 1992.

[20] T.-S. Wang. Multidimensional Unstructured-Grid Liquid Rocket-Engine Nozzle Performance and Heat Transfer Analysis. *Journal of Propulsion and Power*, 22(1):78–84, jan 2006.

[21] H. Elbanna and J. A. Sabbagh. Interaction of two nonequal plane parallel jets. *AIAA Journal*, 25(1):12–13, jan 1987.

[22] A. Durve, A. W. Patwardhan, I. Banarjee, G. Padmakumar, and G. Vaidyanathan. Numerical investigation of mixing in parallel jets. *Nuclear Engineering and Design*, 242:78–90, 2012.

[23] C.-L. Chang, Y. Kronzon, and C. L. Merkle. Time-iterative solutions of viscous supersonic nozzle flows. *AIAA Journal*, 26(10):1208–1215, oct 1988.

[24] K. Shimura, Y. Asako, and J. H. Lee. NUMERICAL ANALYSIS FOR SUPERSONIC FLOWS IN A COOLED NOZZLE. *Numerical Heat Transfer, Part A: Applications*, 26(6):631–641, dec 1994.